Influence of magnetic boundary conditions on the quantitative modelling of magnetorheological elastomers

Miguel Angel Moreno-Mateos, Kostas Danas, Daniel Garcia-Gonzalez

Mechanics of Materials 184 (2023) 104742

Contents lists available at ScienceDirect

Mechanics of Materials

journal homepage: www.elsevier.com/locate/mecmat

Editor invited article

Influence of magnetic boundary conditions on the quantitative modelling of magnetorheological elastomers

Miguel Angel Moreno-Mateos [a,b,*], Kostas Danas [c,*], Daniel Garcia-Gonzalez [a,*]

[a] Department of Continuum Mechanics and Structural Analysis, Universidad Carlos III de Madrid, Avda. de la Universidad 30, 28911 Leganés, Madrid, Spain
[b] Institute of Applied Mechanics, Friedrich-Alexander-Universität Erlangen–Nürnberg, Egerlandstr. 5, 91058 Erlangen, Germany
[c] LMS, C.N.R.S, École Polytechnique, Institut Polytechnique de Paris, Palaiseau, 91128, France

ARTICLE INFO

Dataset link: https://zenodo.org/record/8129310

Keywords:
Computational mechanics
Magneto-mechanics
Magnetorheological elastomers
Magnetostriction
Boundary conditions

ABSTRACT

The complex magneto-mechanical coupling that governs the material response of magnetorheological elastomers (MREs) requires computational tools to assist the design process. Computational models are usually based on finite element frameworks that often simplify and idealise the magnetic source and the associated magnetic boundary conditions (BCs). However, these simplifications may lead to important disagreement between the actual material behaviour and the modelled one, even at the qualitative level. In this work, we provide a comprehensive study on the influence of magnetic BCs and demonstrate the importance of considering them in the overall material-structure modelling strategy. To this end, we implement a magneto-mechanical framework to model the response of soft- and hard-magnetic MREs under magnetic fields generated by an idealised far-field uniform magnetic source, a permanent magnet, a coil system, and an electromagnet with two iron poles. The results unveil remarkable heterogeneities in computed local magnetostriction and magnetic fields depending on the magnetic setup used. A detailed discussion based on material and structural contributions provides a robust, rigorous, and necessary modelling route for future works.

1. Introduction

Magnetorheological elastomers (MREs) are attracting tremendous attention due to their ability to mechanically respond to external magnetic stimuli. Numerous state-of-the-art applications lie in their abilities to modify their mechanical properties and to perform functional shape changes. Among others, soft actuators (Moreno-Mateos et al., 2022b), functional substrates for mechanobiology studies (Moreno-Mateos et al., 2022a), drug delivery systems, surface patterning (Psarra et al., 2017, 2019), and metastructures (Lum et al., 2016; Danas, 2017; Kim et al., 2018; Alapan et al., 2020; Montgomery et al., 2021) take advantage of such features. MREs consist of an elastomeric matrix filled with magnetic particles that, under magnetic actuation, provide a magneto-mechanical coupled response (Danas et al., 2012; Bodelot et al., 2018; Metsch et al., 2021; Silva et al., 2022; Moreno-Mateos et al., 2023; Saber and Sedaghati, 2023). In turn, the fillers can have either soft (i.e. fully energetic) or hard (i.e. dissipative) magnetisation response. On the one hand, soft-magnetic MREs (sMREs) are ideal to tune the mechanical properties of the composite under magnetic actuation. This relates to the so-called magnetorheological effect (Stepanov et al., 2013; Vatandoost et al., 2020). On the other hand, hard-magnetic MREs (hMREs), which are naturally anisotropic due to the pre-existing permanent magnetisation direction, offer a remarkable shape-morphing capability owing mainly to significant magnetic torque mechanisms,[1] (Kalina et al., 2017; Moreno-Mateos et al., 2022c; Zhang et al., 2023).

In general terms, the manufacturing parameters of magneto-active structures clearly determine the functional response of the composite influencing magnetorheological, magnetostrictive, and torque effects. Some of these factors include the type and amount of magnetic fillers, the stiffness of the matrix, and the microstructural arrangement of the fillers within the matrix (Kalina et al., 2016, 2020b). However, despite being the microstructural parameters determinant to tune the material response, there are two additional macroscopic factors that are crucial: (i) the magneto-mechanical boundary conditions (BCs) and (ii) the geometry of the magneto-responsive structure (Keip and Rambausek,

Invited Editor: Daniel Rittel.

* Corresponding authors.
E-mail addresses: migmoren@ing.uc3m.es (M.A. Moreno-Mateos), konstantinos.danas@polytechnique.edu (K. Danas), danigarc@ing.uc3m.es (D. Garcia-Gonzalez).

[1] The shape-morphing capability of hMREs lies in the transmission of torques from the pre-magnetised particles to the soft matrix (Moreno-Mateos et al., 2022c,b, 2023; Garcia-Gonzalez et al., 2023).

https://doi.org/10.1016/j.mechmat.2023.104742
Received 23 May 2023; Received in revised form 1 July 2023; Accepted 1 July 2023
Available online 7 July 2023

2016; Lefèvre et al., 2017; Keip and Rambausek, 2017; Rambausek and Danas, 2021).

To fully grasp the macroscopic response of the MRE, it is paramount to comprehend the interplay of microscopic structural formations and their interactions across various local areas of the sample (Lefèvre et al., 2017; Lefèvre et al., 2020). In some recent works, the authors Danas (2017), Mukherjee et al. (2020), Lucarini et al. (2022) delved into the effects of the structural interplays and their competition with microstructural mechanisms. A set of experiments characterised the macroscopic behaviour while a homogenisation framework provided insights into the microstructural mechanisms. In that study, and in qualitative agreement with alternative experiments in a different magnetic setup (Bodelot et al., 2018), an intriguing point was that the experimental sMRE samples expanded under magnetic actuation whereas the homogenisation results predicted compression of the medium. Based on such observations as well as on earlier research combining homogenisation models and structural boundary value simulations (Lefèvre et al., 2017), the work of Lucarini et al. (2022) confirmed the necessity to explicitly reproduce as realistically as possible the actual macroscopic boundary conditions. In this respect, several works showed the importance of describing the entire boundary value problem (BVP) of the experimental setup (Zhao et al., 2011; Ju et al., 2012; Lefèvre et al., 2017; Dorn et al., 2021; Moreno-Mateos et al., 2022a). This enables the understanding of the actual effect of the magnetic field and the straightforward comparison of the experimental and numerical results. Overall, the previous studies emphasised the importance of modelling the real magnetic BCs to recreate the functional response of MREs.

The most common approach to study magneto-mechanical problems is the assumption of ideal homogeneous magnetic fields (Biro and Preis, 1989; Kalina et al., 2020a; Dadgar-Rad and Hossain, 2022). However, such an interpretation of the magnetic field may lead to significant deviations from the experimental observations with real actuation setups. Therefore, an important question arises on whether the explicit representation of the BCs is needed depending on the analysis to be performed. The idealisation of the external magnetic field is appropriate to study the intrinsic material properties, uncouple them from structural influences and understand the microstructural deformation mechanisms of MREs (Danas, 2017). Nevertheless, the study of a combined material-structural response under realistic magnetic actuation requires a comprehensive approach, i.e., a complete model including the MRE sample, the magnetic source and the surrounding air. In this more complete approach, the geometry of the sample together with the material characteristics play a critical role in the heterogeneous deformations and the potential formation of structural instabilities (Danas and Triantafyllidis, 2014; Psarra et al., 2017, 2019; Zhang and Rudykh, 2022; Li et al., 2022).

The object of this work is to provide a roadmap on the computational modelling of real magneto-mechanical problems. We restrict attention to simplified constitutive frameworks, while we maintain full three-dimensional finite element (FE) implementations to highlight the importance of the BCs on the magnetostriction of MREs with regard to the macroscopic problem addressed. To this end, we consider four different magnetic actuation setups: (1) a homogeneous far-applied, idealised magnetic field, (2) a field induced by permanent magnets, (3) a coil system mimicking those used in most magnetorheology devices, and (4) an electromagnet with two iron poles with fairly uniform fields in the mid-section but in a finite domain. The four approaches are implemented and tested to actuate s/hMRE samples with different, albeit simple cylindrical geometries. The results are then compared to experimental data allowing to uncover significant differences in the magnetostriction and the formation of interesting instabilities leading to complex deformations.

2. Modelling framework

In this section, we propose a simplified energetic formulation for s/hMREs. The formulation has its roots in more complete ones including nonlinear magnetic response (Mukherjee et al., 2020), magnetic dissipation (Mukherjee et al., 2021) as well as viscoelasticity (Garcia-Gonzalez and Hossain, 2021a; Lucarini et al., 2022; Rambausek et al., 2022). While the proposed numerical setting can be used to address all those cases, in the present study the interest lies in small magnetic fields and mechanically very soft MREs. The goal is to analyse the relative magnetic interactions between the MRE and the surrounding boundary conditions. For this reason, we restrict our attention to a simplified, but otherwise sufficient, model which allows to analyse the main experimental observations at hand.

2.1. Constitutive model

The deformation of MREs is modelled at finite strains. The deformation gradient $\mathbf{F} = \boldsymbol{\nabla}_0 \mathbf{u} + \mathbf{I}$ and its Jacobian $J = \det(\mathbf{F})$ are the kinematic entities of the medium Ω_0 and its boundary $\partial\Omega_0^{\mathrm{T}}$, with $\mathbf{u}$ denoting the displacement field, $\boldsymbol{\nabla}_0$ the gradient in the material (reference) configuration, and $\mathbf{I}$ the second-order identity tensor. Moreover, the magnetic problem uses a vector-potential formulation to model the electric current density ($\mathbf{J}$) on the coil (Biro and Preis, 1989; Dorn et al., 2021). The definition of the magnetic induction from a vector-potential field as $\mathbb{B} = \boldsymbol{\nabla}_0 \times \mathbf{A}$, with $\boldsymbol{\nabla}_0 \times$ denoting the curl operator in the material configuration, is specially adequate because $\mathbf{A}$ is the work conjugate of $\mathbf{J}$. Therefore, the resulting primary fields of the problem are $\mathbf{u}$ and $\mathbf{A}$.

Using an eddy current approximation, which consists in neglecting the electric displacement currents in the Maxwell equations (Ammari et al., 2000), one may define the total potential energy as the sum of the internal energy, the work done by the electric currents, the body forces ($\mathbf{f}$), and the traction forces ($\mathbf{T}$) as

$$\begin{aligned}\Pi = &\int_{\Omega_0} \Psi(\mathbf{F}, \mathbb{B})\, \mathrm{d}V - \int_{\Omega_0} \mathbf{J} \cdot \mathbf{A}\, \mathrm{d}V - \int_{\Omega_0} \mathbf{f} \cdot \mathbf{u}\, \mathrm{d}V - \int_{\partial\Omega_0^{\mathrm{T}}} \mathbf{T} \cdot \mathbf{u}\, \mathrm{d}S \\ &+ \frac{1}{2\mu_0 \zeta} \int_{\Omega_0} \left(\boldsymbol{\nabla}_0 \cdot \mathbf{A}\right)^2 \mathrm{d}V. \end{aligned} \tag{1}$$

Note that the last term in Eq. (1) introduces the Coulomb gauge constraint $\boldsymbol{\nabla}_0 \cdot \mathbf{A}$, with $\boldsymbol{\nabla}_0 \cdot$ being the divergence in the material configuration, to ensure the uniqueness of the vector potential and its continuity across the phases interfaces (Danas et al., 2019; Dorn et al., 2021). The parameter ζ should be adjusted numerically to be small enough thus acting as a penalty that imposes the Coulomb constraint. In this work, a value of $\zeta = 1{\cdot}10^{-7}$ delivers converged and stable numerical results. The vacuum magnetic permeability is denoted with μ_0.

To obtain the weak form, let us minimise Eq. (1) through the variation of the energy with respect to $\mathbf{u}$ and $\mathbf{A}$

$$\begin{aligned}\delta\Pi = &\int_{\Omega_0} \left(\mathbf{P} \cdot \nabla_0 \delta\mathbf{u} + \mathbb{H} \cdot (\nabla_0 \times \delta\mathbf{A})\right) \mathrm{d}V - \int_{\Omega_0} (\mathbf{J} \cdot \delta\mathbf{A} + \mathbf{f} \cdot \delta\mathbf{u})\, \mathrm{d}V \\ &- \int_{\partial\Omega_0^{\mathrm{T}}} \mathbf{T} \cdot \delta\mathbf{u}\, \mathrm{d}S + \frac{1}{\mu_0 \zeta} \int_{\Omega_0} \left(\boldsymbol{\nabla}_0 \cdot \mathbf{A}\right) \left(\boldsymbol{\nabla}_0 \cdot \delta\mathbf{A}\right) \mathrm{d}V. \end{aligned} \tag{2}$$

Moreover, the constitutive equations to obtain the work conjugates $\mathbf{P}$ and $\mathbb{H}$ can be derived applying the Coleman–Noll framework (Dorfmann and Ogden, 2004)

$$\mathbf{P} = \frac{\partial \Pi}{\partial \mathbf{F}}, \qquad \mathbb{H} = \frac{\partial \Pi}{\partial \mathbb{B}}. \tag{3}$$

Next, let us define the total energy density as the sum of a mechanical, matter magnetisation, and free space (i.e., magnetic vacuum or Maxwell) contributions,

$$\Psi(\mathbf{F}, \mathbb{B}) = \Psi_{\mathrm{mech}} + \Psi_{\mathrm{mag}} + \Psi_{\mathrm{maxw}}. \tag{4}$$

The mechanical contribution is defined with a Gent hyperelastic model and the volumetric contribution from Miehe and Schänzel (2014),

$$\Psi_{\text{mech}}(\mathbf{F}) = -\frac{GJ_{\text{m}}}{2}\ln\left[1-\frac{I_1-3}{J_{\text{m}}}\right]+\frac{G}{\beta}\left(J^{-\beta}-1\right), \tag{5}$$

where $I_1 = \text{tr}\left(\mathbf{F}^{\text{T}}\cdot\mathbf{F}\right)$ is the first mechanical invariant, G the shear modulus of the composite material, J_{m} the stretching threshold, $\beta = 2\nu/(1-2\nu)$, and ν is the Poisson's ratio. We note that one could potentially use a homogenisation model for Ψ_{mech}, e.g., that proposed in Lopez-Pamies et al. (2013). However, the present MREs were shown experimentally to have a quasi-incompressible response with Poisson ratios slightly smaller than 0.5. For this reason, in the present study we identify G and ν with those obtained from the corresponding experiments (see later Table 1).

The matter magnetisation contribution consists of energetic and remanent contributions, defined here as

$$\Psi_{\text{mag}}(\mathbf{F},\mathbb{B}) = \Psi_{\text{mag,e}}+\Psi_{\text{mag,r}} = -\frac{\mu_r-1}{2\mu_0\,\mu_r\,J^2}I_5^{\text{e}}+I_5^{\text{er}}, \tag{6}$$

where μ_r is the relative magnetic permeability, the energetic invariant $I_5^{\text{e}} = (\mathbf{F}\cdot\mathbb{B})\cdot(\mathbf{F}\cdot\mathbb{B})$, and the remanent invariant $I_5^{\text{er}} = \mathbb{B}\cdot\mathbf{C}^{1/2}\cdot\mathcal{H}^r$, with $\mathcal{H}^r$ denoting a remanent magnetic field that *a priori* needs to be evaluated via a complete dissipative framework (Mukherjee et al., 2021; Mukherjee and Danas, 2022).[2] The remanent magnetic field $\mathcal{H}^r$ allows to model more generally the remanent magnetisation of the pre-magnetised hMRE and the permanent magnet. We also note that the proposed function (6) is a reduced version of the more complete energy density proposed in Mukherjee and Danas (2022). Nonetheless, in the present study this version suffices to analyse the boundary condition effects that we are interested in.

Finally, the free space contribution is given by

$$\Psi_{\text{maxw}}(\mathbf{F},\mathbb{B}) = \frac{1}{2\mu_0\,J}I_5^{\text{e}}. \tag{7}$$

Remark. The prescription of a constant $\mathcal{H}^r$ field (per magnetic domain) in (6) implies that the remanent magnetic field or magnetisation is known *a priori*. A more realistic approach would require considering the remanent magnetisation as an internal variable that would evolve during the pre-magnetisation stage according to the BVP, the geometry of the MRE structure and the real distribution of the magnetic field (Mukherjee et al., 2021; Mukherjee and Danas, 2022). Consequently, the previous approach would lead to more intricate and by construction precise pre-magnetisation patterns. Nonetheless, in a number of practical fabrication processes where a magnetiser is used to pre-magnetise a simple MRE geometry, as is the case in this study, a very large magnetic field is applied for a short time leading to almost full saturation and thus an almost constant saturated value of $\mathcal{H}^r$ everywhere in the solid. Therefore, the prescription of $\mathcal{H}^r$ is a perfectly suitable approximation exactly equivalent to that of establishing a per-domain magnetisation profile (Zhao et al., 2019; Yan et al., 2023). In fact, in the absence of an external magnetic field the internal remanent variable $\mathcal{H}^r$ may be directly associated with the Eulerian magnetisation in the current configuration (Mukherjee and Danas, 2022). However, if complex MRE geometries with strong interactions in between different domains are involved, these pre-magnetisation profiles may still remain complex and thus shall not be prescribed in an ad-hoc manner since they may introduce significant errors.

[2] In previous studies, the internal variable was denoted as $\mathcal{H}^r$ in Mukherjee et al. (2021) and as $\boldsymbol{\xi}$ in Mukherjee and Danas (2022). The first notation was originally proposed to denote a remanent H-field in an $\mathbf{F}-\mathbf{H}$ formulation. In the second more recent study, it was shown that the internal variable remains valid and exactly the same in the dual $\mathbf{F}-\mathbf{B}$ formulation. In this work, we will denote with $\mathcal{H}^r$ the internal variable serving to describe a remanent magnetic field similar to the plastic strain in elasto-plasticity models with units those of the H-field and the magnetisation.

Remark. Finally, we note that the energy density (6) leads to a linear magnetic response of sMREs (by setting $\mathcal{H}^r = \mathbf{0}$) and to a linear magnetic response around a pre-magnetised state for hMREs (by setting $\mu_r = 1$). In turn, by setting both $\mu_r = 1$ and $\mathcal{H}^r = \mathbf{0}$, we model non-magnetic domains such as air. Other materials involved in the magnetic source device, such as iron or coils, may be also modelled with the same energy function by assigning corresponding magnetic properties and fairly large mechanical moduli so that no straining is induced therein. Moreover, the proposed model is uncoupled at the pure material scale in the sense discussed by Danas (2017), i.e., when Eulerian background fields are applied at the pure material point. This choice has been done on purpose here such that any observed local magnetostriction, shown in the following section, is a pure consequence of the interaction between the magnetoactive structure and the magnetic boundary conditions.

2.2. Numerical implementation

The FE computations are performed on different meshes, on sMRE and hMRE samples immersed in an air domain and subjected to different magnetic (and mechanical) boundary conditions obtained by modelling directly the magnetic source. These involve an ideal homogeneous field, a permanent magnet, a coil system, and an electromagnet (see Fig. 1) . All these setups establish the same magnetic field magnitude on the base of the sample, but produce a different spatial field distribution.

Ideal domain. The mesh for the ideal homogeneous magnetic actuation has 17,308 elements and consists of a cylindrical MRE sample immersed in a surrounding air domain of dimensions 80 mm × 80 mm × 100 mm (see Fig. 1.A). Next, we employ magnetic Dirichlet BCs on the vector potential $\mathbf{A}$. To this end, we impose on the boundaries of the air domain $\mathbf{A} = \frac{1}{2}B_2X_3\mathbf{e_1} - \frac{1}{2}B_2X_1\mathbf{e_3}$, where X_1 and X_2 are the Cartesian coordinates and B_2 the target ideal magnetic induction to be established on the computation domain. As a consequence, the application of the curl operator on the potential field ($\boldsymbol{\nabla}_0\times\mathbf{A}$) leads to a uniformly magnetic induction field along the $\mathbf{e_2}$ direction.

Permanent magnet. The mesh for the case of a permanent magnet contains 38,122 elements. It consists of three domains: the cylindrical sample, the permanent magnet and the free space (see Fig. 1.B). The cylindrical magnet has a diameter of 20 mm and height of 10 mm, and it is placed so that the magnetic induction on the sample is approximately 200 mT. Both the sample and the magnet are immersed in a cube of 100 mm edge length representing the free space. In this case, all the components of $\mathbf{A}$ are set to zero on the far air boundary. Moreover, the permanent magnetisation of the magnet is prescribed using Eq. (6), with $\mu_0\mathcal{H}^r = 1.1\,\mathbf{e_2}$ T.

Rheometer coil system. The mesh for the coil system has 77,763 tetrahedral elements. Five domains form this mesh: the sample, the lower yoke, the coil, a free space interface between the sample and the plate of the coil system,[3] and the free space (see Fig. 1.C). The inner diameter of the coil is 20 mm, the outer diameter is 40 mm, and the height of the lower yoke, 40 mm. Furthermore, the diameter of the cylindrical free space domain is 100 mm. The numerical simulation takes advantage of partial axial symmetry to reduce the computational domain.[4] All the components of the potential vector are set to zero on the free space boundary and, on the symmetry planes, $\partial A_1/\partial x|_{x=0} = 0$ and $\partial A_3/\partial z|_{z=0} = 0$. However, unlike the models for the homogeneous field and permanent magnet, here a current density $\mathbf{J}$ needs to be applied in the coil. Note that this system reproduces the real conditions in most magnetorheological rheometers, where a close loop controls

[3] In order to allow the free deformation of the MRE sample, a thin interface between the sample and the plate of the coil system is modelled with the same properties of the free space.

[4] Note that rotations of the samples could break down full axisymmetry.

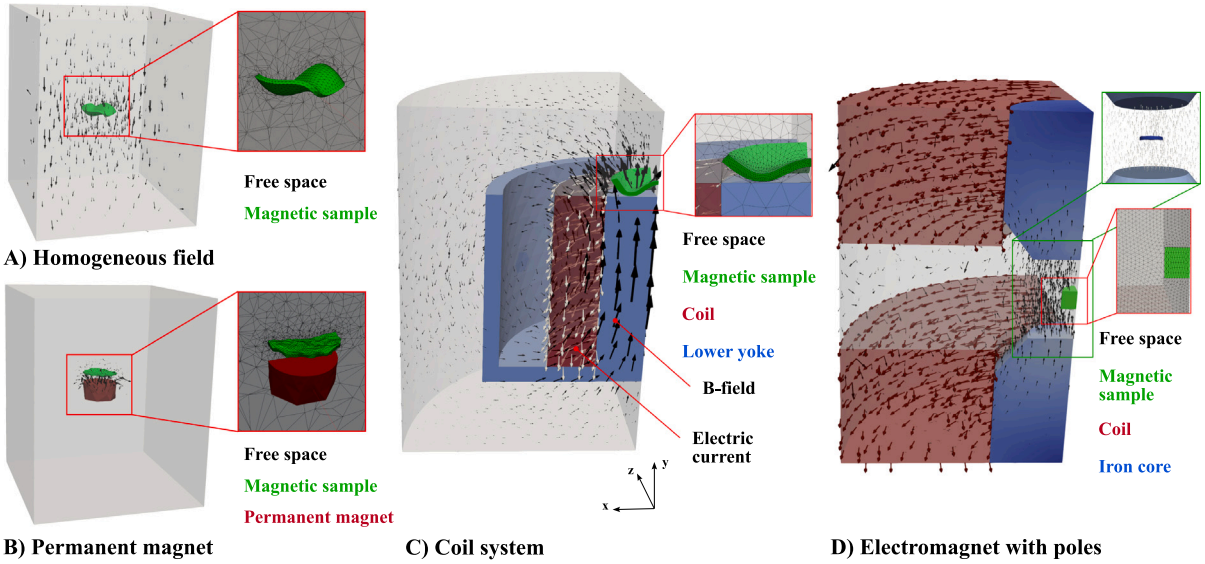

Fig. 1. Numerical domains of the BVPs to prescribe a magnetic field on MRE samples. (A) Ideal homogeneous magnetic field. Two domains compose the mesh: the sample (green colour) and the free space (grey). (B) Magnetic field established by a permanent magnet. The sample (green), the permanent magnet (red) and the free space (grey) form the numerical domain. (C) Coil system in magneto-mechanical rheology setups. The MRE sample (green) deforms under the actuating magnetic field induced by the electric coils (red) in the vertical direction. The lower yoke (blue) of the magnetorheological device provides the structural support for the coils and the sample. Note that it reproduces the experimental setup without the upper yoke. Finally, the free space (grey) surrounds the magnetorheological device and the sample. Note that a thin free space layer between the sample and the yoke allows the free magnetostriction of the sample. (D) Electromagnet with iron poles to establish a vertical magnetic field. The MRE sample (green) immersed in free space (grey) deforms under the magnetic field established by the coils (red) and the iron poles (blue). For all the BVPs, deformed configurations of the samples are shown. (For interpretation of the references to colour in this figure legend, the reader is referred to the web version of this article.)

the current to establish the target magnetic induction to be measured by the Hall probe on the base of the sample, i.e., on the Peltier plate. Consequently, the azimuth current J_θ is adjusted to produce the desired fields. For the three actuating frameworks, the boundary of the free space, the lower yoke and the coils are mechanically fixed.

Electromagnet with iron poles. Finally, the mesh for the electromagnet implements the same approach as the one for the rheometer but includes two iron poles inside the two coil domains (see Fig. 1.D). The poles serve to concentrate and enhance the uniformity and amplitude of the applied magnetic field. The MRE sample is placed between the poles. The inner and outer diameter of the coils are 150 mm and 450 mm, respectively, with a height of 125 mm. The diameter of the iron poles is 90 mm and they are separated by 80 mm. Likewise, the partial axial symmetry of the problem allows to simplify the computational domain. Note that the magnetic field is highly concentrated in the cylindrical domain in-between the two poles, while the coils extend way beyond that cylindrical domain. The magnetic field outside such a virtual cylinder is almost negligible and it is not needed to add more free space beyond the coil. The resulting mesh has 44,604 elements.

For all the aforementioned BVPs, two types of samples are used to analyse structural effects: a slender cylindrical sample with diameter equal to 20 mm and thickness of 1 mm, as well as a bulky cylindrical sample with diameter 4 mm and thickness of 1 mm. In addition, note that the mechanical response of the surrounding air is defined as a compressible material with very low stiffness so that no mechanical constraints were imposed on the MRE sample (Pelteret et al., 2016; Dorn et al., 2021; Moreno-Mateos et al., 2022a,b). For further strategies for the treatment of the contiguous free space, the reader is referred to Rambausek et al. (2022), Rambausek and Schöberl (2023). Apart from the symmetry boundary conditions, no additional boundary conditions need to be prescribed on the samples. These are immersed in the free space and do not experience rigid body motion.

For each sub-domain, Table 1 contains the mechanical and magnetic parameters used in the simulations on sMRE and hMRE samples. For the hMRE case, the pre-magnetisation field is introduced in the solving scheme as an initial linear ramp. Then, it remains constant and the external magnetic field is applied, also as a linear ramp. Note that the mechanical parameters have been obtained from experimental data (Moreno et al., 2021; Moreno-Mateos et al., 2022a), whereas the magnetic ones are determined with the computational homogenisation framework presented in Lucarini et al. (2022). In addition, ϕ denotes the volume fraction of the particles used during the experiments.

3. Results

3.1. Different experimental set-ups induce different deformation modes on MREs exposed to the same magnetic field magnitudes

This section exemplifies that, despite prescribing the same magnitude of the magnetic actuation, different experimental setups may lead to completely different deformation modes, mainly because different magnetic heterogeneity is induced by the various setups locally. To this end, we make use of three experimental systems that generate magnetic fields of 200 mT on MRE samples. However, the nature of the magnetic sources is quite different. Fig. 2 shows the magnetostrictions of sMRE and hMRE, slender and bulky samples for actuation with the permanent magnet, the coil system, and the electromagnet actuation setups. Note that the case of the homogeneous far-field BC is an idealisation, thus not achievable with a real actuation setup. The coil system and electromagnets allow the direct prescription of the magnetic magnitude. In contrast, for the case of the permanent magnet a teslameter was used to place the samples at a certain distance and establish the 200 mT field on the base of the samples. Note, however, that magnetic lines outside a cylindrical magnet tends to rotate very quickly thus inducing gradient magnetic fields.

In order to further demonstrate the role of the magnetic BCs, we actuate samples of different material nature (i.e., sMRE and hMRE) and with different geometries. The results highlight the differences in the magnetostriction of all sample types depending on the magnetic actuation. In particular, hMREs tend to be more unstable than sMREs, as is expected by the significant torques present due to the pre-magnetisation field.

Table 1
Mechanical and magnetic parameters for the BVPs modelled to reproduce the different setups used to magnetically actuate on MRE samples. Note that the values for the effective magnetic permeability are extracted from Lucarini et al. (2022). In addition, the remanent magnetic field is measured with a teslameter on a pre-magnetised hMRE sample. The lower yoke is inherent to the rheometer BVP, the iron poles are implemented in the electromagnet BVP, and the coils, in both.

Type of MRE	Mechanical			Magnetic	
	Shear mod. G [kPa]	Poisson's ν [–]	Strechability J_m [–]	Rel. magnetic permeability μ_r [–]	Remanent magnetic field $\mu_0 \mathcal{H}^r$ [T]
sMRE ($\phi = 0.1$)	1.6	0.47	1.7	1.28	0
sMRE ($\phi = 0.2$)	2.0	0.47	1.7	1.62	0
sMRE ($\phi = 0.3$)	2.9	0.47	1.7	2.1	0
hMRE ($\phi = 0.3$)	2.9	0.47	1.7	1	$15 \cdot 10^{-3}$
Free space	$80 \cdot 10^{-3}$	0.2	2000	1	0
Lower yoke	$1 \cdot 10^3$	0.49	2000	1	0
Coil	$1 \cdot 10^3$	0.49	2000	1	0
Iron pole	$1 \cdot 10^3$	0.49	2000	2000	0
Permanent magnet	$1 \cdot 10^3$	0.49	2000	1	1.1

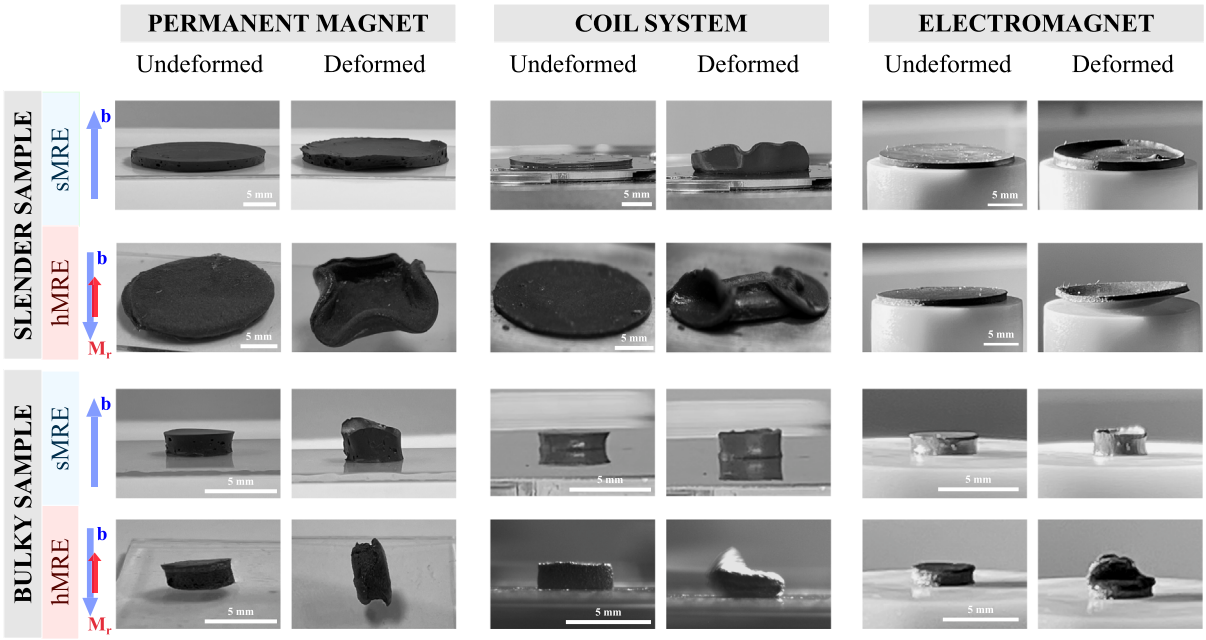

Fig. 2. Empirical overview of the magnetostriction of sMRE and hMRE, slender and bulky samples attending to the magnetic actuation setup. (Left) Magnetic actuation with a permanent magnet. (Middle) Actuation on samples placed on top of the magnetorheological device. The results have been extracted from Lucarini et al. (2022) and Moreno-Mateos et al. (2022c). (Right) Electromagnet with two iron poles to establish a magnetic field in the space between them. The sample is placed in the middle of both magnetic poles. Note that all setups induce a same 200 mT magnetic field on the sample (blue arrows denoting the b-field). hMRE samples are pre-magnetised in the vertical direction (red arrow). (For interpretation of the references to colour in this figure legend, the reader is referred to the web version of this article.)

3.2. Magnetic field lines resulting from magnetic boundary conditions determine MREs deformation modes

Fig. 2 experimentally showed that a sample with a given geometry responds in a different manner under different magnetic boundary conditions. Hereafter, we provide a numerical comparison of the structural deformation of slender and bulky cylindrical samples under four actuation conditions: ideal homogeneous field, permanent magnet, coil system, and electromagnet with iron poles. Every framework is adjusted to establish a magnetic induction on the base of the sample of 200 mT. The frameworks are applied to explore the behaviour of sMREs and hMREs. For the hMRE samples, a constant pre-magnetisation in the vertical direction is prescribed. Consequently, the inner remanent field interacts with the external magnetic field via Zeeman interaction (Garcia-Gonzalez and Hossain, 2021b).

Fig. 3 provides a comprehensive view on the magnetostrictive behaviour of sMRE and hMRE samples, slender and bulky geometries, for the four actuation setups. For the sMRE samples, the deformation under the ideal homogeneous field is almost uniaxial, with a decrease of the diameter and increase of the thickness. The permanent magnet actuation, however, leads to some intricate deformations due to the non perfectly homogeneous magnetic field lines. In turn, the coil system, commonly used in rheometer setups, leads to an interesting vertical bending of the slender sample. Although bending deformation modes are typical for hMREs with remanent magnetisation (transmission of torques from the pre-magnetised particles to the matrix (Moreno-Mateos et al., 2022b)), it can also be obtained with a sMRE and a heterogeneous magnetic field (Psarra et al., 2017, 2019; Lucarini et al., 2022). For this actuation setup, the coil induces a vertical field in the middle region that diverges on the upper region where the sample is placed.

Finally, the electromagnet produces a deformed configuration close to the one obtained with the ideal field. For the hMRE samples, the ideal field produces an interesting structural instability. In an asymmetric manner, one side of the slender sample undergoes convex bending whereas the other performs a concave bending. Unlike this magnetostrictive behaviour, the entire slender sample bends in the same

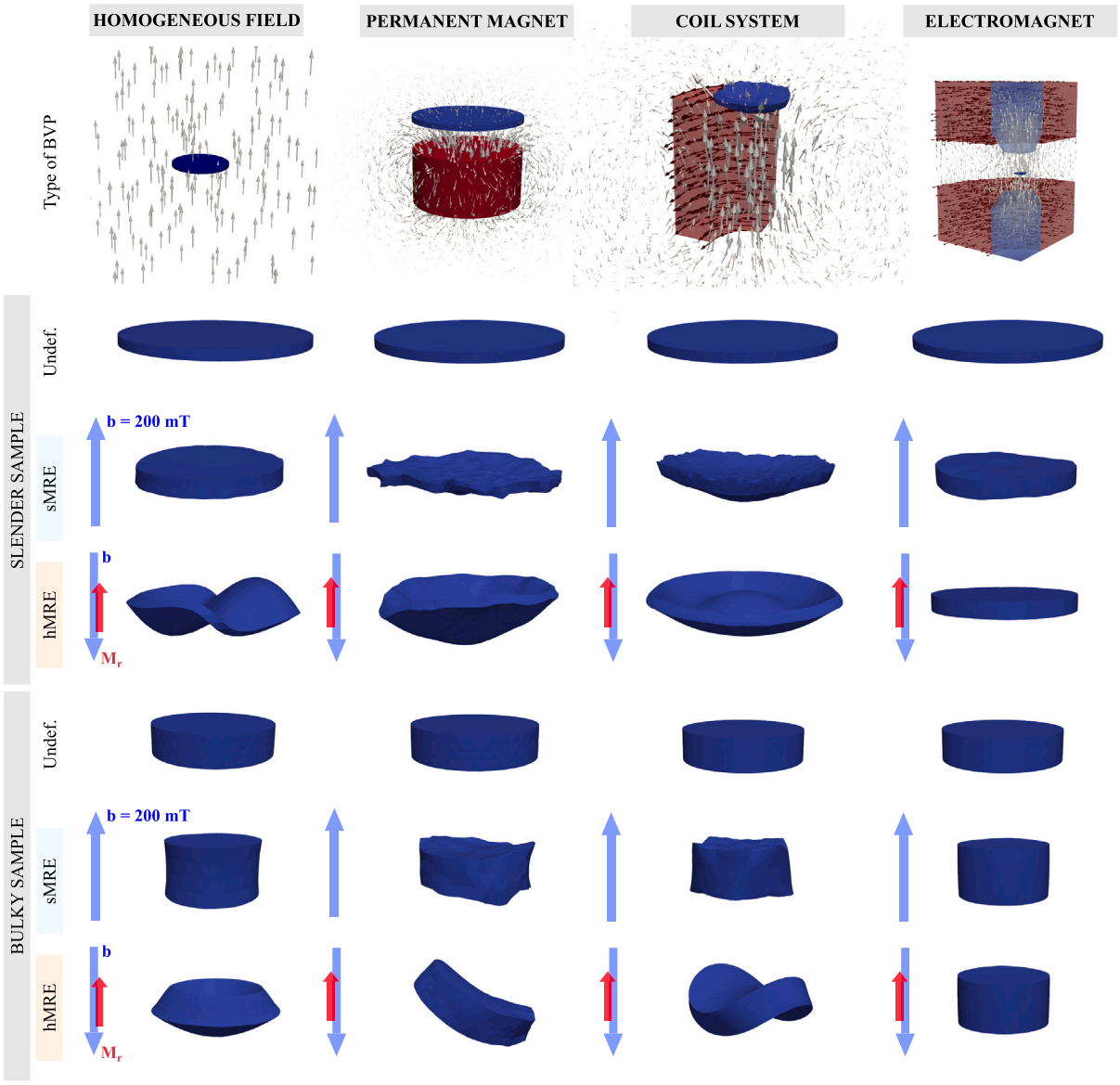

Fig. 3. Influence of magnetic BCs on the magnetostriction of sMRE and hMRE, slender and bulky cylindrical samples. The slender sample has a diameter of 20 mm and the bulky one, a diameter of 4 mm. Both have a common thickness of 1 mm. (Column 1) Magnetostriction of a sMRE and hMRE sample under a 200 mT ideal homogeneous magnetic field. The actuation on the hMRE has the opposite direction with respect to the remanent magnetisation of the sample. (Column 2) Magnetostriction under magnetic actuation with a permanent magnetic. The separation between the sample and the magnet is determined to achieve a 200 mT field on the MRE. (Column 3) Magnetostriction for the actuation with the rheometer setup. The current in the coil induces the magnetic field in the vertical direction. In the upper region, it is not perfectly homogeneous. (Column 4) Magnetostriction for the electromagnet actuation setup for a sample placed in between the magnetic poles. For all the actuation setups, note that the grey arrows on the upper illustration represent the magnetic induction vector ($\mathbb{B}$). Moreover, note that the remanent magnetic field of the hMRE samples is $\mu_0 \mathcal{H}^r = \pm 15\,\mathbf{e}_2$ mT. (For interpretation of the references to colour in this figure legend, the reader is referred to the web version of this article.)

direction when the magnetic field is not perfectly homogeneous. These are the cases for the actuation with the permanent magnet and the coil system. On the contrary, the bulky sample exhibits deformation of the entire MRE, since it tends to macroscopically rotate and align with the field. In addition, the field created with the coil produces an additional instability in the inner region of the slender sample. Overall, the results demonstrate the remarkable effects of the magnetic BCs on the magnetostrictive response of MREs. In this regard, the response of a sMRE can range from a simple, albeit non-uniform, uniaxial deformation to more complex functional deformations (e.g., bending) as long as the magnetic field is not perfectly homogeneous.

3.3. The influence of magnetic boundary conditions is particularly strong on the sample boundary

The non-ideal actuation setups lead to a magnetic field that is not perfectly homogeneous, neither at the free space nor inside the sample. A quantification of the magnetostriction of the bulky sMRE samples is given in Fig. 4. The deformation map (components F_{11} and F_{22}) and the magnetic field (component B_2) are provided for inner $x-z$ and $y-z$ cut planes. In addition, to examine the evolution of the fields with the magnetic loading, the local equivalent strain is plotted versus the magnetic induction at two control points: one at the middle of the

sample and the other at the middle top surface. For the permanent magnet and coil setups, the results reveal significant heterogeneity in both the deformation map and magnetic field.[5]

Within the same plane, B_2 oscillates between 50 mT and 250 mT for the permanent magnet actuation and between 140 mT and 200 mT for the coil configuration. Likewise, the stretch F_{11} varies from 0.7 to 0.95 for the permanent magnet and from 0.7 and 0.85 for the coil setup. In turn, the stretch F_{22} illustrates vertical expansion inside the sample and compression of the edges. Finally, the electromagnet with the two iron poles is the actuation setup that resembles the most ideal homogeneous far-field with the more homogeneous deformation and magnetic fields. In this respect, the deformation only presents some heterogeneity in the peripheral edges. Regarding the evolution of the equivalent strain with the magnetic actuation, it begins with a quadratic form, reaching saturation fairly fast at larger magnetic fields.

3.4. Homogeneous remanent magnetisation in hMREs leads to heterogeneous magnetic fields and deformations even under external homogeneous magnetic fields

The immersion of a hMRE sample with remanent magnetisation in a homogeneous magnetic field generates heterogeneities in the magnetic and deformation fields. To quantify this effect, Fig. 5 includes plots of the B_2-field and the F_{22}-field on bulky hMRE samples under homogeneous magnetic actuation and the permanent magnet setup. In addition, Fig. 5.c shows, for homogeneous magnetic actuation, the B_2-field on a cross-section cut of the complete computational domain: hMRE and free space. While the field is homogeneous far from the sample, it becomes heterogeneous in the magnetic sample and neighbouring free space. Note that we impose here a small B-field actuation of 50 mT to show that, even at low magnetic fields, mechanical and magnetic heterogeneities appear. Overall, these results highlight the need to accurately account for real magnetic BCs and solve the coupled magneto-mechanical problem.

3.5. Structural effects associated with sample geometry influence MRE deformation modes

The magnetostriction is usually driven by structural effects, i.e., macroscopic interactions between different domains of the material. The influence of such geometrical effects were experimentally illustrated by the authors in a previous work (Lucarini et al., 2022) where slender and bulky cylindrical sMRE samples were tested on the coil system under free deformation conditions (see Fig. 6). While the bulky samples performed an almost uniaxial reduction of the diameter and increase of the thickness, the slender disks exhibited a more complex deformation, namely bending. To explain such a behaviour, the authors discussed the mechanisms of paramagnetic torques, which drive the formation of chains of particles and their alignment with the external magnetic field. In order to further demonstrate the need for the *in silico* reproduction of the magnetic BCs and the geometry of the structure, next we apply the framework introduced in the previous sections to mimic the deformation modes of samples with alternative geometries. We compare the virtual results with the experimental counterparts. Note that all structures are actuated with a magnetorheological device (i.e., coil system).

We begin with nine simulations on sMRE disks with diameters of 4 mm, 6 mm, and 20 mm and magnetic particles' contents of $\phi = \{0.1, 0.2, 0.3\}$ (see Fig. 6). For the 4 mm and 6 mm disks, we quantify the magnetostriction as the engineering overall vertical strain. The smaller disk undergoes a larger vertical deformation than the 6 mm one, with values of 42 %, 57 % and 59 % from the lowest particles' content to the highest. In turn, the 6 mm disk presents values of 38 %, 40 %, and 56 % strain. Moreover, the larger the diameter of the disk, the larger the structural effects, i.e., the disk undergoes bending in its peripheral regions, which tend to align with the external magnetic field. Given that the slenderness of the structures is a crucial factor influencing the formation of instabilities, we report additional simulations varying the thickness of the sMRE samples (1 mm and 0.5 mm), see Fig. 6. The 0.5 mm one leads to smaller axial deformation and larger bending. Overall, these results agree qualitatively well to the experimental findings, demonstrating that the implementation of the entire BVP and its magnetic BCs is paramount to properly link the constitutive framework to the real behaviour. Especially, it is important when non-uniform deformations are shown to be the rule in spite of substantial efforts to have uniform fields in the sample.

Unlike sMREs, hMREs with remanent magnetisation show more complex magnetostriction even under homogeneous magnetic fields. This is a direct result of the transmission of torques from the particles to the elastomeric matrix. Next, we report additional simulations for two bending disks (4 mm and 20 mm diameter) and a bending beam that mimic the experimental specimens reported by the authors in Moreno-Mateos et al. (2022c). The deformation of the hMRE samples under reverse magnetic actuation uncover interesting tendencies (see Fig. 7.A). The bending disks perform two structural instabilities depending on the diameter. The first one, for the smaller disk, may be described as a saddle-like instability; whereas the second one, for the larger disk, resembles a wave-like deformation. Moreover, the deformation of the beam can be categorised as a twisting deformation mode. For all these cases, the deformation is such that the pre-magnetisation vector tends to align with respect to the external magnetic induction.

As a final consideration, we explore the performance of a gripper actuator whose behaviour lies in the magneto-mechanical coupling of MREs. Traditionally, these structures have been prepared with hard-magnetic particles to perform functional morphological changes (Becker et al., 2018; Xu et al., 2019; Song et al., 2020; Xu et al., 2021; Ze et al., 2020). Related to these applications, we implement a four-arm actuator and apply the magnetic actuation with the coil system framework. The implementation of both sMRE and hMRE configurations provides guidance for the choice of the type of magnetic particles. The results for the deformation of the gripper in Fig. 7.B show that, although the hMRE allows for more intricate shape changes than the sMRE actuator, a remarkable bending is obtained with the sMRE configuration. This behaviour owes to the non-homogeneous nature of the magnetorheological device used for the magnetic actuation, which produces the macrostructural arrangement of the sample with the field lines despite lacking the remanent magnetisation of hMREs that typically drives torques.

4. Discussion and conclusion

Numerous previous works in the literature addressing the modelling of MREs under magnetic actuation sometimes reported controversial results. In this regard, it is sometimes unclear if, under external magnetic actuation, a MRE sample should compress, elongate or undergo an even more complex mechanical response. In this work, we have experimentally demonstrated that samples using the same material and geometry can respond differently to magnetic stimuli with *a priori* same magnitude (Fig. 2). An extended argument in the literature to explain such discrepancies relates to the microstructural distribution of magnetic particles within the MRE (Boczkowska and Awietj, 2012; Kalina et al., 2020a; Romeis et al., 2019). These works suggest that contraction

[5] The coil system, commonly used in magnetorheological devices, has been used without the upper yoke to allow free deformation conditions. This produces the heterogeneities in the magnetic field that drive the structural effects in the magnetostriction of shMRE samples. On the contrary, when the upper yoke is used, the magnetic field is fairly homogeneous in all the middle space where the sample is placed. This setup was previously used by the authors to perform the rheological characterisation of ultra-soft sMRE samples (Moreno et al., 2021). In this regard, Appendix shows the spatial $\mathbb{b}$-field obtained with an additional simulation.

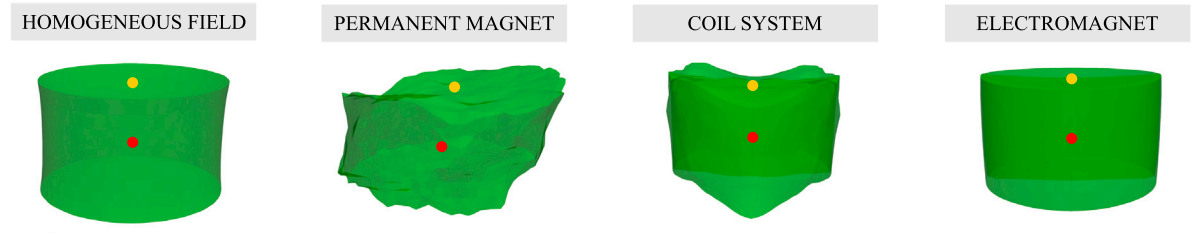

a) Bulky **sMRE samples** deformed under magnetic actuation and indication of two pointsat the center middle (red) and top middle (orange).

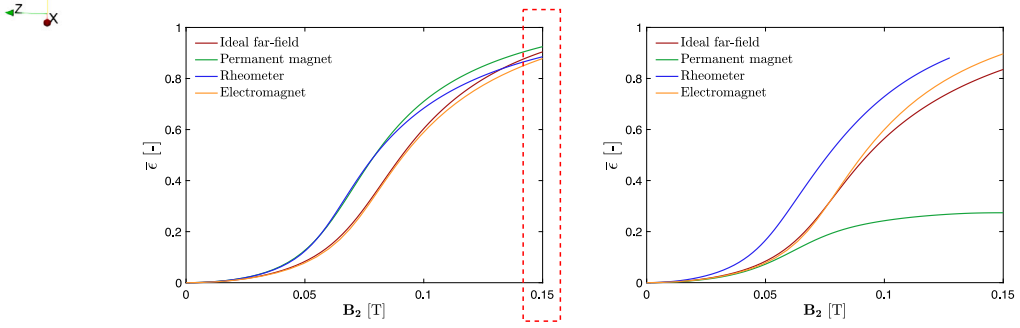

b) Local equivalent strain as a function of the vertical magnetic induction at (left) middle (red) point and (right) top (orange) point.

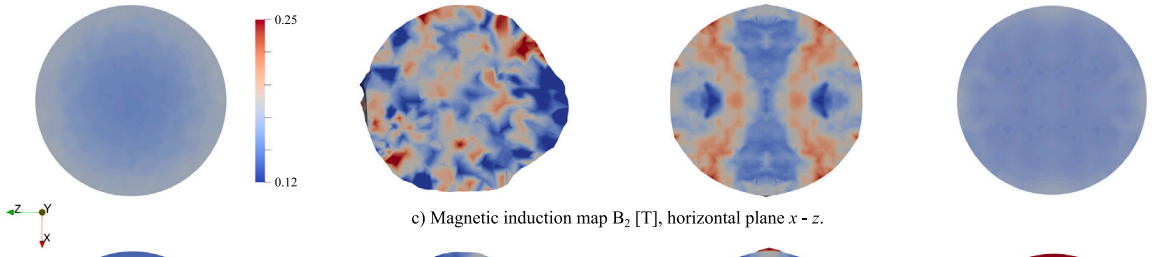

c) Magnetic induction map B_2 [T], horizontal plane x - z.

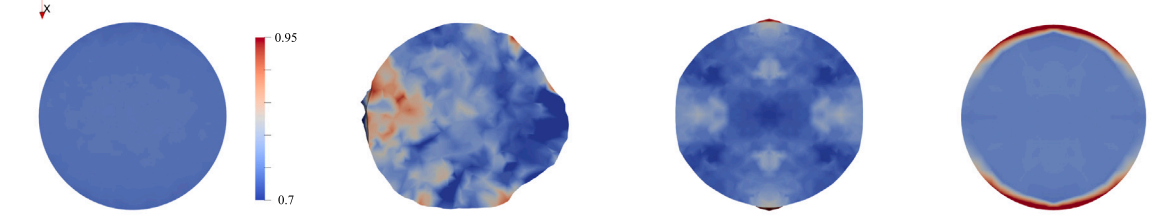

d) Mechanical deformation map F_{11} [-], horizontal plane x - z.

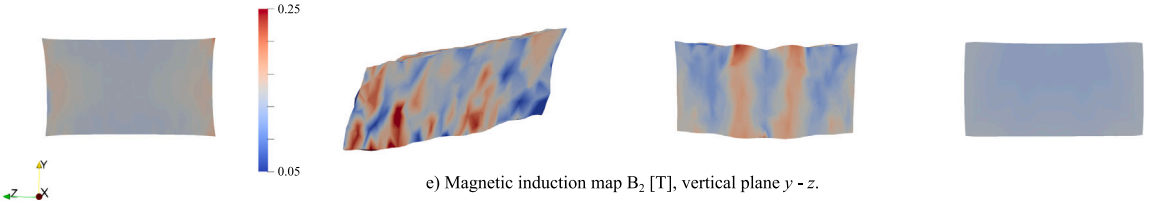

e) Magnetic induction map B_2 [T], vertical plane y - z.

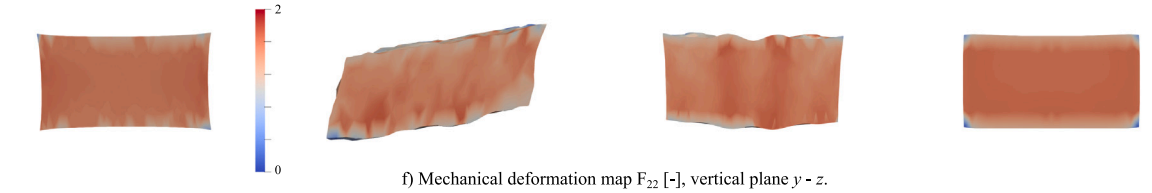

f) Mechanical deformation map F_{22} [-], vertical plane y - z.

Fig. 4. Quantification of the magnetostriction of bulky sMRE samples for the different magnetic actuation BCs. (a) Deformed configuration of the samples for a vertical magnetic induction of 150 mT. (b) Evolution of the equivalent strain with the B_2 component at a middle point and a top-middle point. The equivalent stress is defined as $\epsilon = \sqrt{\frac{2}{3}\mathbf{E} : \mathbf{E}}$, with $\mathbf{E} = \frac{2}{3}[\mathbf{C} - \mathbf{I}]$. (c) Contour plots of the component B_2 of the magnetic induction for a $x-z$ cross-section at half the height of the cylindrical sample. (d) Contours plots of the component F_{11} of the deformation gradient for a $x-z$ cross-section at half the height of the cylindrical sample. (e) Contour plots of the component B_2 of the magnetic induction for a $y-z$ cross-section at the middle of the cylindrical sample. (f) Contours plots of the component F_{22} of the deformation gradient for a $y-z$ cross-section at the middle of the cylindrical sample. (For interpretation of the references to colour in this figure legend, the reader is referred to the web version of this article.)

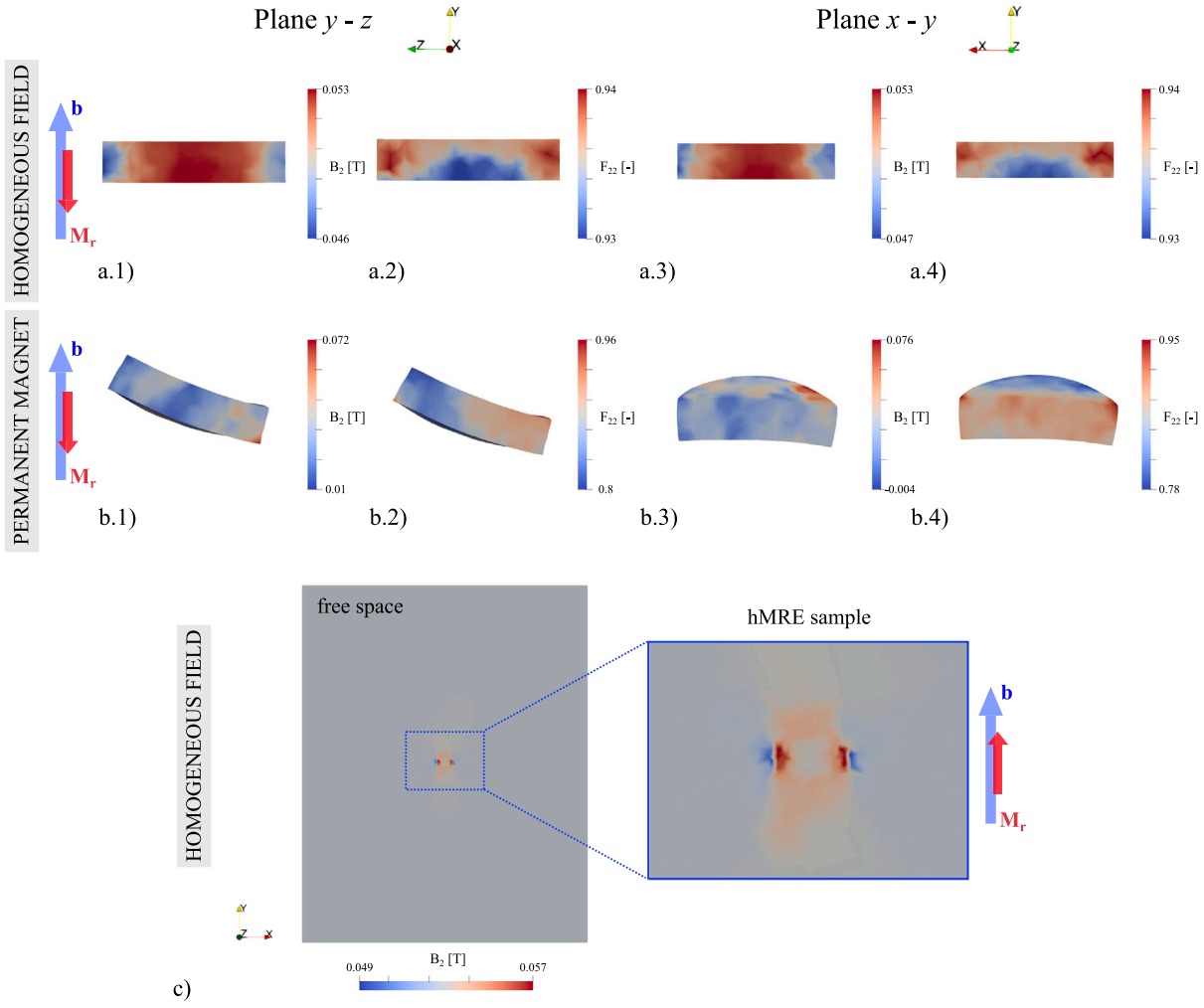

Fig. 5. Quantification of the magnetostriction of bulky hMRE samples for the ideal magnetic actuation and the permanent magnet setup. (a.1-4) Contour plots of the B_2-field and F_{22}-field for $y-z$ and $x-y$ cross-sections of the cylindrical samples under ideal homogeneous magnetic actuation. The remanent magnetisation ($\mu_0\mathcal{H}^r = 15\,\mathbf{e}_2$ mT) and the magnetic induction vectors have opposite directions. (b.1-4) Contour plots of the component B_2 of the magnetic induction and the component F_{22} of the deformation gradient for $y-z$ and $x-y$ cross-section of the cylindrical samples for the permanent magnet setup. The permanent magnetisation and the magnetic induction have opposite directions. (c) Vertical component B_2 of the magnetic induction field on the hMRE sample and the surrounding air to show the heterogeneity on the $\mathbb{B}$-field on the pre-magnetised sample and the contiguous air. The pre-magnetisation and the magnetic induction have the same direction. (For interpretation of the references to colour in this figure legend, the reader is referred to the web version of this article.)

occurs when the particles are anisotropically aligned and expansion when they are isotropically arranged. Along this idea, other authors have also explored the sign of the magnetostrictive deformation using also a microstructural viewpoint (Danas et al., 2012; Ivaneyko et al., 2014; Gao and Wang, 2019; Fischer and Menzel, 2019; Garcia-Gonzalez and Hossain, 2021a). In an attempt to reconcile both experimental and computational observations, in Lucarini et al. (2022) we presented a microstructural study focused on the interplay between magnetic and viscohyperelastic responses. One of the conclusions was that, to faithfully reproduce the magneto-mechanical problem, the computational model must account for the magnetic BCs by explicitly incorporating the magnetic sources.

In the current work, we demonstrate that the magnetic BCs and nature of the applied field are the primary factors determining the macroscopic response of soft MREs. We offer a comprehensive overview of the magnetostrictive behaviour of sMREs and hMREs under various magnetic boundary conditions. Special attention is drawn to the implications of the actuating magnetic field and the geometry of the MRE structure on their deformation. To this end, we have implemented a numerical framework that mimics ideal homogeneous magnetic actuation and three frameworks reproducing real actuation setups. These are the actuation with a permanent magnet, with a coil system commonly used in magnetorheological devices, and with an electromagnet with two iron poles. In addition, the use of slender and bulky samples allows to examine the formation of instabilities. These results are compared to equivalent empirical ones to stress the importance of reproducing the entire boundary value problem and not mislead the connection between constitutive modelling and the empirical structural behaviour. Overall, the coupled response of the MRE has to be understood as the competition of microscopic particle–particle and particle-matrix interactions and macrostructural interactions between different domains of the MRE sample (Gao et al., 2012; Danas, 2017; Romeis et al., 2019; Gao and Wang, 2019; Wang et al., 2020).

Real magnetic actuation setups and the inhomogeneous nature of the magnetic field result in a more complex magnetostrictive response of sMREs, as demonstrated by the sMRE gripper actuator in Fig. 7.B. Undoubtedly, far from being a penalty, this can inspire not only the design of the magneto-responsive material, but also the nature of magnetic fields used for its actuation. Existing works prove that the design of heterogeneous magnetic fields is an excellent driver to achieve responsive MREs (Moreno-Mateos et al., 2022a). Simultaneously, the design of multi-material structures with different magnetic domains can help achieve more sophisticated deformations (Kim et al., 2018; Lopez-Donaire et al., 2022). Guided by complete computational frameworks,

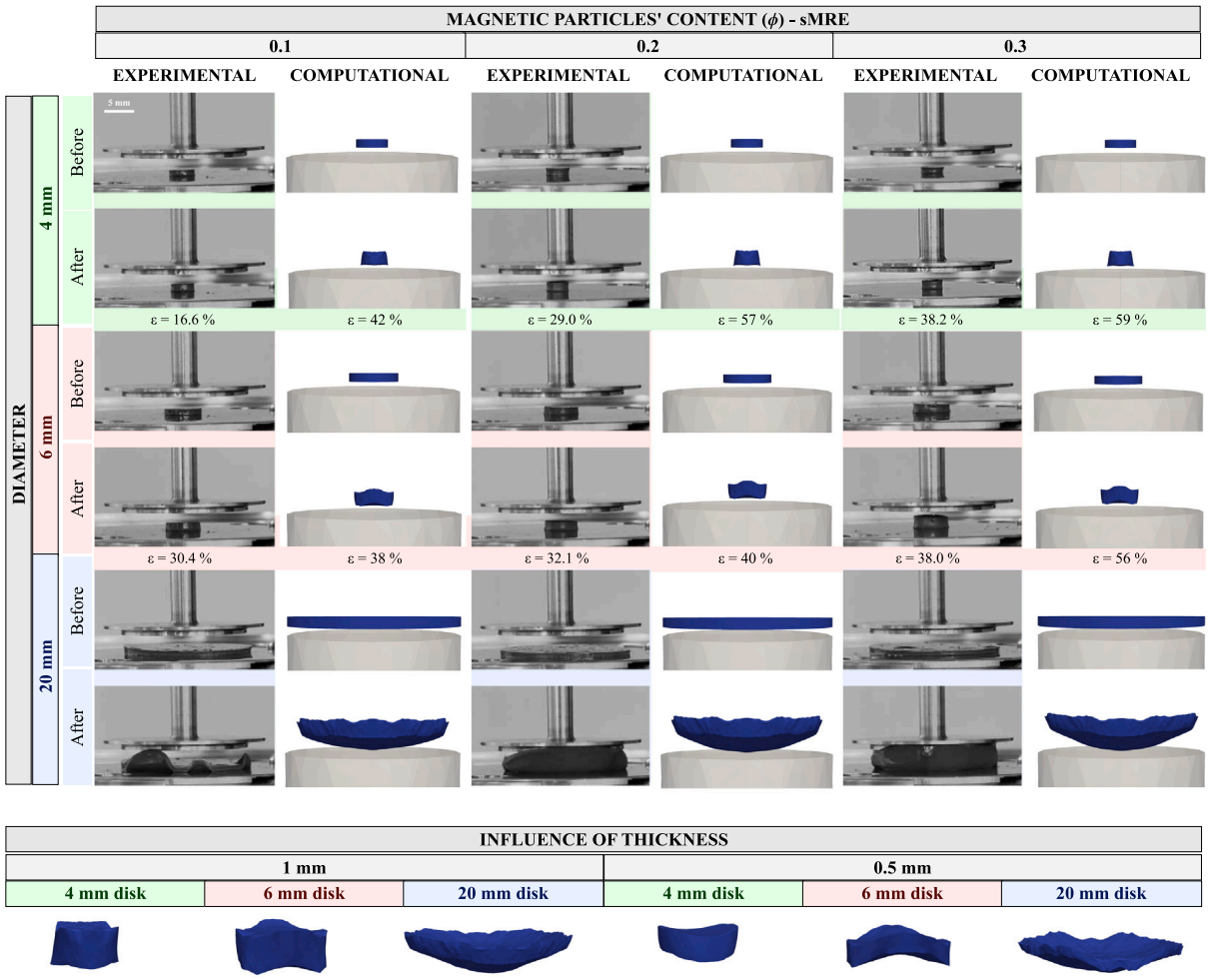

Fig. 6. Comparison of the *in silico* magnetostriction of cylindrical sMRE samples with experimental results for magnetic actuation with a magnetorheological device equipped with a coil system. The computational results display the deformed samples (blue) and the lower plate of the rheometer (grey). The experimental results have been extracted from Lucarini et al. (2022). The cylinders have diameters of 4 mm, 6 mm, and 20 mm, thickness of 1 mm and magnetic particles volume ratios (ϕ) of 0.1, 0.2, and 0.3. The shear moduli and magnetic permeabilities for the sMRE and hMRE and magnetic particles' contents are taken from Table 1. In addition, the magnetic induction on the base of the sample is 300 mT. For the 4 mm and 6 mm samples, the vertical (engineering) strain quantifies the vertical expansion. Moreover, the computational framework is applied to explore the influence of the thickness on the magnetostriction of sMRE samples: the magnetostriction of three sMRE cylindrical samples with 4 mm, 6 mm, 20 mm diameter and thicknesses of 1 mm and 0.5 mm is compared. The results for the thinner samples suggest a more unstable behaviour. (For interpretation of the references to colour in this figure legend, the reader is referred to the web version of this article.)

further approaches may consider other magnetic actuation setups and the pre-magnetisation process of hMRE structures. As reported by Ren et al. (2019) (see also simulations in Mukherjee et al. (2021), Mukherjee and Danas (2022)), heterogeneous pre-magnetisation patterns would allow for higher flexibility in the design of magnetostrictive s/hMRE structures. In this regard, non-uniformly pre-magnetised slender soft actuators can perform a functional magnetostriction even for low magnetic actuations, which prevents the evolution of the remanent magnetisation and the magnetic dissipation (Mukherjee et al., 2021). Moreover, the connection of the present work with FE2 homogenisation schemes would help understand the connection between micro- and macro-scales (Kalina et al., 2022). The comparison of our approach with these microstructural models would help understand the structural effects, such as fringe effects on edges (Zabihyan et al., 2020).

CRediT authorship contribution statement

Miguel Angel Moreno-Mateos: Conceptualisation, Implementation, Formal analysis, Visualisation, Writing – original draft, Writing – review & editing. **Kostas Danas:** Conceptualisation, Formal analysis, Writing – review & editing, Funding acquisition. **Daniel Garcia-Gonzalez:** Conceptualisation, Formal analysis, Writing – review & editing, Funding acquisition.

Declaration of competing interest

The authors declare the following financial interests/personal relationships which may be considered as potential competing interests: Daniel Garcia-Gonzalez reports financial support was provided by European Research Council. Kostas Danas reports financial support was provided by European Research Council.

Data availability

The code developed in this work is available via zenodo in https://zenodo.org/record/8129310. Further data will be made available on request.

Acknowledgements

MAMM and DGG acknowledge support from the European Research Council (ERC) under the European Union's Horizon 2020 research and innovation programme and Horizon Europe programme (Grants -No. 947723 and 101081713). MAMM acknowledges support from the Ministerio de Ciencia, Innovacion y Universidades, Spain (FPU19/03874). KD acknowledges support from the European Research Council (ERC) under the Horizon Europe programme (Grant-No. 101081821).

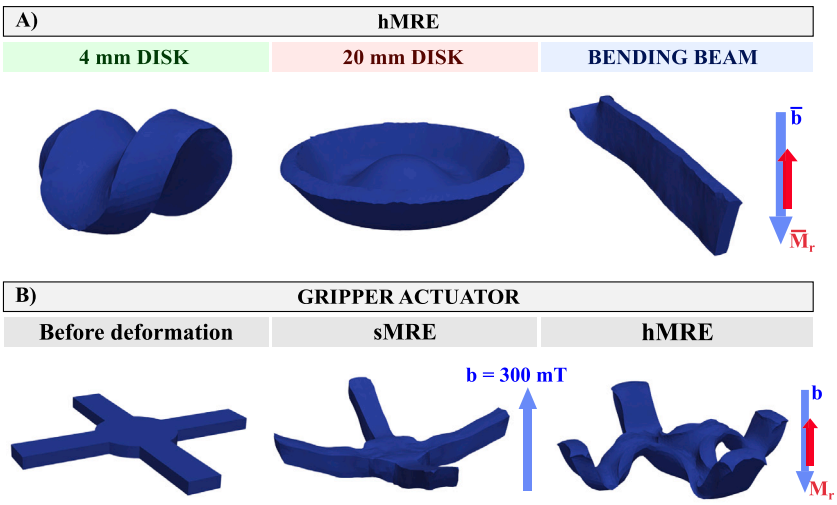

Fig. 7. Computational magnetostriction of hMRE samples for reverse magnetic actuation with the magnetorheological device equipped with a coil system and application of a sMRE and hMRE four-arm gripper. (A.Left) A cylindrical sample with 4 mm diameter and 1 mm thickness exhibits a saddle-like instability. (A.Centre) A 20 mm diameter disk shows a wave-like deformation. (A.Right) A cantilever beam of 20 mm length and 5 mm width is twisted under magnetic actuation. Moreover, the magnetic induction on the lower plate of the rheometer is of 300 mT and the remanent magnetisation of the hMRE samples is $\mu_0 \mathcal{H}^r = -15\,\mathbf{e}_2$ mT. (B.Left) The gripper actuator before magnetic actuation, (B.Centre) sMRE gripper actuator under an upwards magnetic field, and (B.Right) hMRE gripper actuator with an upwards pre-magnetisation $\mu_0 \mathcal{H}^r = -15\,\mathbf{e}_2$ mT and a downwards magnetic field. The magnetic induction of $\mathbb{b} = -300\,\mathbf{e}_2$ mT is measured at the based of the MRE sample to mimic the hall probe in the real rheometer.

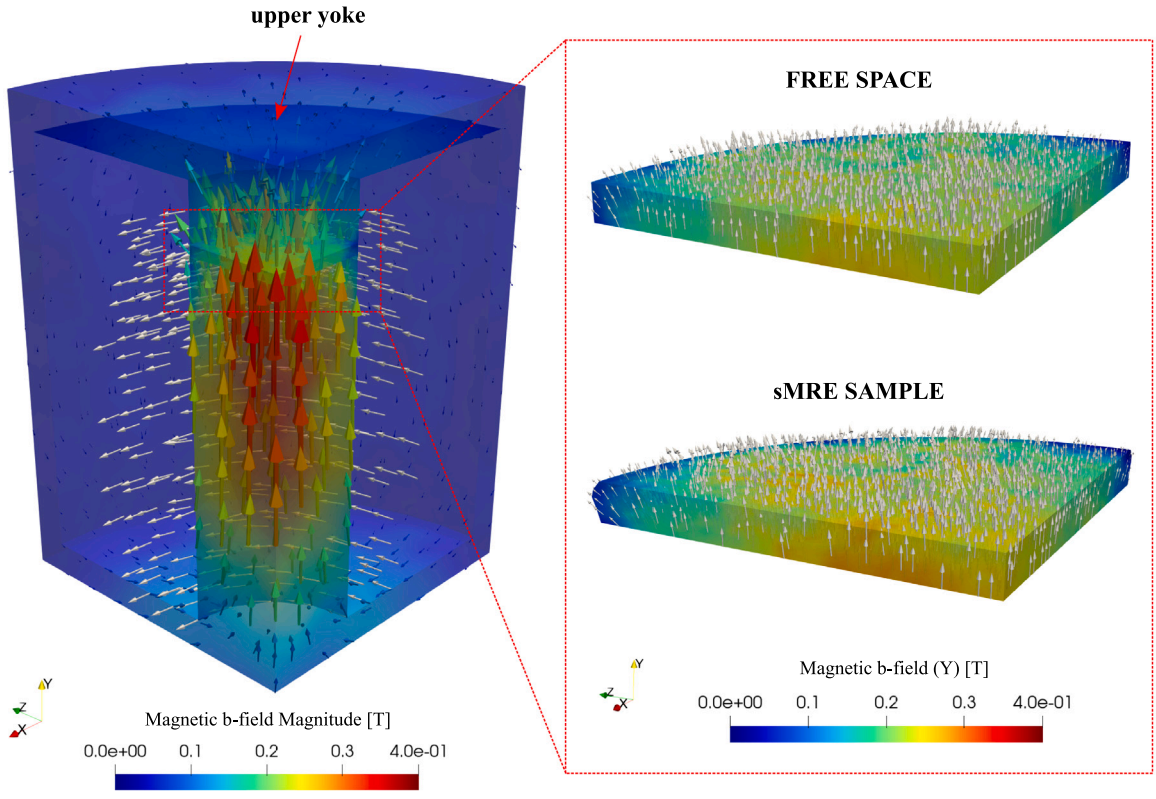

Fig. 8. Homogeneous magnetic actuation with the magnetorheological device equipped with a coil system when using the upper yoke to confine the magnetic field. Magnetic induction for (a) free space between the upper and lower plates and for (b) a sMRE sample placed in the gap. The yoke is modelled with a magnetic permeability of $\mu_r = 5$ and $G = 1 \cdot 10^3$ kPa. Note that the free space is not visualised to facilitate the interpretation of the results. (For interpretation of the references to colour in this figure legend, the reader is referred to the web version of this article.)

Appendix. Magnetorheological device with the upper yoke

The magnetorheological device has been used without the upper yoke to allow for free deformation conditions. This produces the heterogeneities in the magnetic field that drive the structural effects in the magnetostriction of s/hMRE samples. When the upper yoke is used, the magnetic field is fairly homogeneous in all the middle space where the sample is placed. This set up was previously used by the authors to perform the rheological characterisation of ultra-soft sMRE samples (Moreno et al., 2021). To illustrate the homogeneity of the field when the upper yoke is used, Fig. 8 shows the $\mathbb{b}$-field on a middle cut.

References

Alapan, Y., Karacakol, A.C., Guzelhan, S.N., Isik, I., Sitti, M., 2020. Reprogrammable shape morphing of magnetic soft machines. Sci. Adv. 6.

Ammari, H., Buffa, A., Nédélec, J.-C., 2000. A justification of eddy currents model for the maxwell equations. SIAM J. Appl. Math. 60 (5), 1805–1823.

Becker, T., Zimmermann, K., Borin, D., Stepanov, G., Storozhenko, P., 2018. Dynamic response of a sensor element made of magnetic hybrid elastomer with controllable properties. J. Magn. Magn. Mater. 449, 77–82.

Biro, O., Preis, K., 1989. On the use of the magnetic vector potential in the finite-element analysis of three-dimensional eddy currents. IEEE Trans. Magn. 25, 3145–3159.

Boczkowska, A., Awietj, S., 2012. Microstructure and properties of magnetorheological elastomers. Adv. Elast. - Technol. Propert. Appl. 9.

Bodelot, L., Voropaieff, J.-P., Pössinger, T., 2018. Experimental investigation of the coupled magneto-mechanical response in magnetorheological elastomers. Exp. Mech. 58, 207–221.

Dadgar-Rad, F., Hossain, M., 2022. A micropolar shell model for hard-magnetic soft materials. International Journal for Numerical Methods in Engineering 12.

Danas, K., 2017. Effective response of classical, auxetic and chiral magnetoelastic materials by use of a new variational principle. J. Mech. Phys. Solids 105, 25–53.

Danas, K., Kankanala, S., Triantafyllidis, N., 2012. Experiments and modeling of iron-particle-filled magnetorheological elastomers. J. Mech. Phys. Solids 60, 120–138.

Danas, K., Mukherjee, D., Haldar, K., Triantafyllidis, N., 2019. Bifurcation analysis of twisted liquid crystal bilayers. J. Mech. Phys. Solids 123, 61–79.

Danas, K., Triantafyllidis, N., 2014. Instability of a magnetoelastic layer resting on a non-magnetic substrate. J. Mech. Phys. Solids 69, 67–83.

Dorfmann, A., Ogden, R., 2004. Nonlinear magnetoelastic deformations of elastomers. Acta Mech. 167, 13–28.

Dorn, C., Bodelot, L., Danas, K., 2021. Experiments and numerical implementation of a boundary value problem involving a magnetorheological elastomer layer subjected to a nonuniform magnetic field. J. Appl. Mech. 88.

Fischer, L., Menzel, A.M., 2019. Magnetostriction in magnetic gels and elastomers as a function of the internal structure and particle distribution. J. Chem. Phys. 151, 114906.

Gao, Y., Hulsen, M.A., Kang, T.G., den Toonder, J.M.J., 2012. Numerical and experimental study of a rotating magnetic particle chain in a viscous fluid. Phys. Rev. E 86, 041503.

Gao, W., Wang, X., 2019. Experimental and theoretical investigations on magnetoelastic shear behavior of isotropic mr elastomers under gradient magnetic fields. J. Magn. Magn. Mater. 483, 196–204.

Garcia-Gonzalez, D., Hossain, M., 2021a. A microstructural-based approach to model magneto-viscoelastic materials at finite strains. Int. J. Solids Struct. 208-209, 119–132.

Garcia-Gonzalez, D., Hossain, M., 2021b. Microstructural modelling of hard-magnetic soft materials: Dipole–dipole interactions versus Zeeman effect. Extreme Mech. Lett. 48, 101382.

Garcia-Gonzalez, D., Ter-Yesayants, T., Moreno-Mateos, M.A., Lopez-Donaire, M.L., 2023. Hard-magnetic phenomena enable autonomous self-healing elastomers. Composites B 248, 110357.

Ivaneyko, D., Toshchevikov, V., Saphiannikova, M., Heinrich, G., 2014. Mechanical properties of magneto-sensitive elastomers: unification of the continuum-mechanics and microscopic theoretical approaches. Soft Matter 10, 2213–2225.

Ju, B.X., Yu, M., Fu, J., Yang, Q., Liu, X.Q., Zheng, X., 2012. A novel porous magnetorheological elastomer: preparation and evaluation. Smart Mater. Struct. 21, 035001.

Kalina, K.A., Brummund, J., Metsch, P., Kästner, M., Borin, D.Y., Linke, J.M., Odenbach, S., 2017. Modeling of magnetic hystereses in soft mres filled with ndfeb particles. Smart Mater. Struct. 26, 105019.

Kalina, K.A., Linden, L., Brummund, J., Metsch, P., Kästner, M., 2022. Automated constitutive modeling of isotropic hyperelasticity based on artificial neural networks. Comput. Mech. 69, 213–232.

Kalina, K.A., Metsch, P., Brummund, J., Kästner, M., 2020a. A macroscopic model for magnetorheological elastomers based on microscopic simulations. Int. J. Solids Struct. 193-194, 200–212.

Kalina, K.A., Metsch, P., Kästner, M., 2016. Microscale modeling and simulation of magnetorheological elastomers at finite strains: A study on the influence of mechanical preloads. Int. J. Solids Struct. 102-103, 286–296.

Kalina, K.A., Rassloff, A., Wollner, M., Metsch, P., Brummund, J., Kästner, M., 2020b. Multiscale modeling and simulation of magneto-active elastomers based on experimental data. Phys. Sci. Rev. 12.

Keip, M.-A., Rambausek, M., 2016. A multiscale approach to the computational characterization of magnetorheological elastomers. Internat. J. Numer. Methods Engrg. 107, 338–360.

Keip, M.-A., Rambausek, M., 2017. Computational and analytical investigations of shape effects in the experimental characterization of magnetorheological elastomers. Int. J. Solids Struct. 121, 1–20.

Kim, Y., Yuk, H., Zhao, R., Chester, S.A., Zhao, X., 2018. Printing Ferromagnetic Domains for Untethered Fast-Transforming Soft Materials, Vol. 558. Nature Publishing Group.

Lefèvre, V., Danas, K., Lopez-Pamies, O., 2017. A general result for the magnetoelastic response of isotropic suspensions of iron and ferrofluid particles in rubber, with applications to spherical and cylindrical specimens. J. Mech. Phys. Solids 107, 343–364.

Lefèvre, V., Danas, K., Lopez-Pamies, O., 2020. Two families of explicit models constructed from a homogenization solution for the magnetoelastic response of mres containing iron and ferrofluid particles. Int. J. Non-Linear Mech. 119, 103362.

Li, J., Slesarenko, V., Rudykh, S., 2022. Emergence of instability-driven domains in soft stratified materials. Npj Comput. Mater. 8, 100.

Lopez-Donaire, M.L., de Aranda-Izuzquiza, G., Garzon-Hernandez, S., Crespo-Miguel, J., la Torre, M.F., Velasco, D., Garcia-Gonzalez, D., 2022. Computationally guided diw technology to enable robust printing of inks with evolving rheological properties. Adv. Mater. Technol. 2201707.

Lopez-Pamies, O., Goudarzi, T., Danas, K., 2013. The nonlinear elastic response of suspensions of rigid inclusions in rubber: II—a simple explicit approximation for finite-concentration suspensions. J. Mech. Phys. Solids 61 (1), 19–37.

Lucarini, S., Moreno-Mateos, M.A., Danas, K., Garcia-Gonzalez, D., 2022. Insights into the viscohyperelastic response of soft magnetorheological elastomers: Competition of macrostructural versus microstructural players. Int. J. Solids Struct. 256, 111981.

Lum, G.Z., Ye, Z., Dong, X., Marvi, H., Erin, O., Hu, W., Sitti, M., 2016. Shape-programmable magnetic soft matter. Proc. Natl. Acad. Sci. 113, E6007–E6015.

Metsch, P., Romeis, D., Kalina, K.A., Raßloff, A., Saphiannikova, M., Kästner, M., 2021. Magneto-mechanical coupling in magneto-active elastomers. Materials 14, 434.

Miehe, C., Schänzel, L.-M., 2014. Phase field modeling of fracture in rubbery polymers. part i: Finite elasticity coupled with brittle failure. J. Mech. Phys. Solids 65, 93–113.

Montgomery, S.M., Wu, S., Kuang, X., Armstrong, C.D., Zemelka, C., Ze, Q., Zhang, R., Zhao, R., Qi, H.J., 2021. Magneto-mechanical metamaterials with widely tunable mechanical properties and acoustic bandgaps. Adv. Funct. Mater. 31, 2005319.

Moreno, M.A., Gonzalez-Rico, J., Lopez-Donaire, M.L., Arias, A., Garcia-Gonzalez, D., 2021. New experimental insights into magneto-mechanical rate dependences of magnetorheological elastomers. Composites B 224, 109148.

Moreno-Mateos, M.A., Gonzalez-Rico, J., Nunez-Sardinha, E., Gomez-Cruz, C., Lopez-Donaire, M.L., Lucarini, S., Arias, A., Muñoz-Barrutia, A., Velasco, D., Garcia-Gonzalez, D., 2022a. Magneto-mechanical system to reproduce and quantify complex strain patterns in biological materials. Appl. Mater. Today 27, 101437.

Moreno-Mateos, M.A., Hossain, M., Steinmann, P., Garcia-Gonzalez, D., 2022b. Hybrid magnetorheological elastomers enable versatile soft actuators. Npj Comput. Mater. 8, 162.

Moreno-Mateos, M.A., Hossain, M., Steinmann, P., Garcia-Gonzalez, D., 2023. Hard magnetics in ultra-soft magnetorheological elastomers enhance fracture toughness and delay crack propagation. J. Mech. Phys. Solids 173, 105232.

Moreno-Mateos, M.A., Lopez-Donaire, M.L., Hossain, M., Garcia-Gonzalez, D., 2022c. Effects of soft and hard magnetic particles on the mechanical performance of ultra-soft magnetorheological elastomers. Smart Mater. Struct. 31, 065018.

Mukherjee, D., Bodelot, L., Danas, K., 2020. Microstructurally-guided explicit continuum models for isotropic magnetorheological elastomers with iron particles. Int. J. Non-Linear Mech. 120, 103380.

Mukherjee, D., Danas, K., 2022. A unified dual modeling framework for soft and hard magnetorheological elastomers. Int. J. Solids Struct. 111513.

Mukherjee, D., Rambausek, M., Danas, K., 2021. An explicit dissipative model for isotropic hard magnetorheological elastomers. J. Mech. Phys. Solids 151, 104361.

Pelteret, J.-P., Davydov, D., McBride, A., Vu, D.K., Steinmann, P., 2016. Computational electro-elasticity and magneto-elasticity for quasi-incompressible media immersed in free space. Internat. J. Numer. Methods Engrg. 108, 1307–1342.

Psarra, E., Bodelot, L., Danas, K., 2017. Two-field surface pattern control via marginally stable magnetorheological elastomers. Soft Matter 13, 6576–6584.

Psarra, E., Bodelot, L., Danas, K., 2019. Wrinkling to crinkling transitions and curvature localization in a magnetoelastic film bonded to a non-magnetic substrate. J. Mech. Phys. Solids 133, 103734.

Rambausek, M., Danas, K., 2021. Bifurcation of magnetorheological film–substrate elastomers subjected to biaxial pre-compression and transverse magnetic fields. Int. J. Non-Linear Mech. 128, 103608.

Rambausek, M., Mukherjee, D., Danas, K., 2022. A computational framework for magnetically hard and soft viscoelastic magnetorheological elastomers. Comput. Methods Appl. Mech. Engrg. 391, 114500.

Rambausek, M., Schöberl, J., 2023. Curing spurious magneto-mechanical coupling in soft non-magnetic materials. Internat. J. Numer. Methods Engrg. 2.

Ren, Z., Hu, W., Dong, X., Sitti, M., 2019. Multi-functional soft-bodied jellyfish-like swimming. Nature Commun. 10, 2703.

Romeis, D., Toshchevikov, V., Saphiannikova, M., 2019. Effects of local rearrangement of magnetic particles on deformation in magneto-sensitive elastomers. Soft Matter 15, 3552–3564.

Saber, A., Sedaghati, R., 2023. The modeling of magnetorheological elastomers: A state-of-the-art review. Adv. Eng. Mater..

Silva, J., Gouveia, C., Dinis, G., Pinto, A., Pereira, A., 2022. Giant magnetostriction in low-concentration magnetorheological elastomers. Composites B 110125.

Song, H., Lee, H., Lee, J., Choe, J.K., Lee, S., Yi, J.Y., Park, S., Yoo, J.-W., Kwon, M.S., Kim, J., 2020. Reprogrammable ferromagnetic domains for reconfigurable soft magnetic actuators. Nano Lett. 20, 5185–5192.

Stepanov, G.V., Kramarenko, E.Y., Semerenko, D.A., 2013. Magnetodeformational effect of the magnetoactive elastomer and its possible applications. J. Phys. Conf. Ser. 412, 012031.

Vatandoost, H., Hemmatian, M., Sedaghati, R., Rakheja, S., 2020. Dynamic characterization of isotropic and anisotropic magnetorheological elastomers in the oscillatory squeeze mode superimposed on large static pre-strain. Composites B 182, 107648.

Wang, Z., Wang, K., Tang, X., 2020. Heterogeneous magnetic micropillars for regulated bending actuation. Extreme Mech. Lett. 38, 100734.

Xu, C., Yang, Z., Lum, G.Z., 2021. Small-scale magnetic actuators with optimal six degrees-of-freedom. Adv. Mater. 33, 2100170.

Xu, T., Zhang, J., Salehizadeh, M., Onaizah, O., Diller, E., 2019. Millimeter-scale flexible robots with programmable three-dimensional magnetization and motions. Science Robotics 4.

Yan, D., Aymon, B.F., Reis, P.M., 2023. A reduced-order, rotation-based model for thin hard-magnetic plates. J. Mech. Phys. Solids 170, 105095.

Zabihyan, R., Mergheim, J., Pelteret, J., Brands, B., Steinmann, P., 2020. Fe2 simulations of magnetorheological elastomers: influence of microscopic boundary conditions, microstructures and free space on the macroscopic responses of mres. Int. J. Solids Struct. 193–194.

Ze, Q., Kuang, X., Wu, S., Wong, J., Montgomery, S.M., Zhang, R., Kovitz, J.M., Yang, F., Qi, H.J., Zhao, R., 2020. Magnetic shape memory polymers with integrated multifunctional shape manipulation. Adv. Mater. 32, 1906657.

Zhang, Q., Cherkasov, A.V., Xie, C., Arora, N., Rudykh, S., 2023. Nonlinear elastic vector solitons in hard-magnetic soft mechanical metamaterials. Int. J. Solids Struct. 280, 112396.

Zhang, Q., Rudykh, S., 2022. Magneto-deformation and transverse elastic waves in hard-magnetic soft laminates. Mech. Mater. 169, 104325.

Zhao, X., Kim, J., Cezar, C.A., Huebsch, N., Lee, K., Bouhadir, K., Mooney, D.J., 2011. Active scaffolds for on-demand drug and cell delivery. Proc. Natl. Acad. Sci. 108, 67–72.

Zhao, R., Kim, Y., Chester, S.A., Sharma, P., Zhao, X., 2019. Mechanics of hard-magnetic soft materials. J. Mech. Phys. Solids 124, 244–263.